

# Microstructural degradation of polycrystalline superalloys from oxidized carbides and implications on crack initiation

Paraskevas Kontis<sup>a,\*</sup>, David M. Collins<sup>b</sup>, Angus J. Wilkinson<sup>b</sup>, Roger C. Reed<sup>b</sup>, Dierk Raabe<sup>a</sup>, Baptiste Gault<sup>a</sup>

<sup>a</sup> Max-Planck-Institut für Eisenforschung, Max-Planck-Str. 1, 40237 Düsseldorf, Germany.

<sup>b</sup> Department of Materials, University of Oxford, Parks Road, OX1 3PH, Oxford, UK.

## Abstract

Surface connected MC carbides in a polycrystalline superalloy oxidised at 750 °C in air were studied because of their potential as crack initiation sites. Lattice rotations measured in the  $\gamma/\gamma'$  grains using high-resolution electron backscatter diffraction enabled investigation of the plastic deformation induced solely by the oxidation of an MC carbide. Dislocations were found to enhance  $\gamma'$  precipitate dissolution kinetics, resulting in soft recrystallised regions in the vicinity of the oxidised carbide. Atom probe tomography revealed a substantial compositional variation between recrystallised grains and the original  $\gamma/\gamma'$  microstructure. Ramifications of such deleterious oxidised carbides alongside soft recrystallised regions on the crack initiation life in superalloys are discussed.

**Keywords:** oxidised carbides, recrystallisation, atom probe tomography,  $\gamma'$  dissolution

MC-type carbides are known to serve as crack initiation sites under fatigue conditions at elevated temperatures in nickel-based superalloys by acting as stress concentration sites [1]. These inherently brittle particles cannot easily accommodate plastic deformation when subjected to high stresses, instead failing through fracture or decohesion from the  $\gamma/\gamma'$  microstructure. Micro-cracks originating from these loci may subsequently propagate [2]. When tested under complex stress and temperature cycles, the cracks may instead initiate in regions close to a free surface, originating from an oxidised MC carbide, and subsequently propagate within the bulk [3,4]. The products from the oxidation of the MC carbides result in their volume expansion, subsequently generating significant local plastic deformation [5]. Nevertheless, the exact mechanism for crack initiation by oxidised carbides is not well understood. For instance, it is not clear to what extent the localised plastic deformation occurs and whether the composition of the  $\gamma/\gamma'$  microstructure can be potentially altered.

Advanced characterisation techniques that offer spatially resolved quantification of deformation and composition now enable the mechanisms governing oxidised carbide failure to finally be investigated. Specifically, the combination of high-resolution electron backscatter diffraction (HR-EBSD) permitting plasticity quantification can be linked to composition measurements made using atom probe tomography (APT). From HR-EBSD, plastic deformation is inferred by quantifying the geometrically necessary dislocation (GND) density and distribution [6], based upon measurements of the lattice curvature and subsequent analysis of the Nye tensor [7]. This experimental method has previously been applied to superalloys to study the accumulation of GND fields near grain boundaries and non-metallic inclusions [8,9]. APT analysis of oxide particles and oxide scales from superalloys, oxide dispersion-strengthened ferritic alloys and steels have been successfully characterised giving accurate chemical composition data [10–15].

In this study, a polycrystalline superalloy IN792, commonly used in industrial gas turbines, was investigated. The chemical composition of the alloy is Ni-13.9Cr-8.8Co-1.1Mo-1.3W-7.6Al-4.9Ti-1.3Ta-0.4C-0.1B-0.012Zr (at.%). The material was supplied by Howmet in the form of conventionally cast round bars of diameter 20 mm. The as-cast bars were hot isostatically pressed (HIP) at 1195 °C and 150 MPa for 2 hours followed by solution heat treatment at 1121 °C for 2 hours. The final stage of ageing was conducted at 850 °C for 24 hours. Specimens were ground and polished with abrasive media to a 1  $\mu\text{m}$  finish from a fully heat treated bar and were isothermally and statically exposed at 750 °C for 50 hours (i.e. under no external mechanical loading).

A dual column scanning electron and focused ion beam (SEM-FIB) Zeiss NVision 40 microscope was used for the initial surface observations. In addition, HR-EBSD was utilised to reveal the details of the plastic

localisation in the vicinity of an oxidised MC carbide. First, a nickel layer was electrochemically deposited on the oxidised surface prior to sample preparation. The cross-section of the statically-exposed specimen was polished to a 0.04  $\mu\text{m}$  colloidal silica finish. A JEOL 6500F field emission gun-scanning electron (FEG-SEM) microscope operating with a 20 keV accelerating voltage and a beam current of  $\sim 14$  nA and equipped with a TSL Digiview II Peltier-cooled charge coupled device (CCD) was used. From a selected region of interest, an EBSD map with an area  $14 \times 10 \mu\text{m}^2$  with a step size of 0.05  $\mu\text{m}$  was collected. EBSD patterns were recorded at full resolution ( $1000 \times 1000$  pixel) with an exposure time of 0.5 s and were saved for offline analysis. Using an in-house analysis method to quantify lattice curvature, the geometrically necessary dislocation (GND) density was estimated [6]. The exact crystallographic information of the oxidised and non-oxidised MC carbides is not known and could not be inferred from this investigation, hence these areas of the GND map are blanked.

In order to investigate any chemical variations between the recrystallised grains and the adjacent deformed  $\gamma/\gamma'$  microstructure, APT specimens were prepared from site-specific lift-outs from recrystallised regions and within the deformed  $\gamma/\gamma'$  microstructure, using a dual column SEM-FIB FEI Helios 600 following procedures described in Ref. [16]. Specimens were analysed on a Cameca LEAP 3000 HR instrument operating in laser pulsing mode with a repetition rate of 100 kHz, laser pulse energy 0.6 nJ and at a base temperature of 70 K. In addition, APT specimens were produced from the MC carbide in the heat treated condition and after the static exposure, in order to investigate alterations in its composition.

Surface eruptions caused by the oxidation of MC carbides connected to the surface in the polished, unstressed specimens are clearly illustrated in Figure 1a. Both inter- and intragranular carbides oxidise as long as they are located close or connected to the surface, as shown in Figure 1b. Similar surface observations of oxidised MC carbides in samples that were similarly statically exposed to various temperatures in air have previously been reported [8,17,18]. Further investigation of the intergranular carbide shown in detail in Figure 1c has revealed the formation of pores within the bulk of the specimen. A FIB cross-section of the intergranular oxidised carbide is shown in Figure 1d, in which the formation of pores due to the oxidation of the carbide is apparent. It is believed that pores are forming due to the outward formation of the oxide products towards the free surface. The pores have formed after only 50 hours of static exposure at 750 °C in the absence of any external applied stress. Pores are known to serve as stress concentration sites where cracks can initiate in superalloys [19]. Thus, our observations give a first strong indication that cracks can primarily initiate within or in the vicinity of oxidised MC carbides.

The oxidation of the MC carbides was confirmed by APT analysis. Table 1 provides the compositions measured by APT of two MC carbides, one after heat treatment and one after isothermal static exposure in air at 750 °C for 50 hours. In the IN792 alloy, the MC carbide was initially found to be Ti/Ta-rich, with other elements such as molybdenum and tungsten present in smaller concentrations. After thermal exposure, the chemistry of the MC carbide was altered substantially. In Figure 1e, an APT reconstruction from an oxidised MC carbide is shown. Two regions with different concentrations of Ti, Ta and O were found which likely correspond to  $\text{TiO}_2$  and  $(\text{Ti,Ta})_2\text{O}_5$ . An elemental composition profile measured as a function of the distance from the  $\text{TiO}_2/(\text{Ti,Ta})_2\text{O}_5$  interface (i.e. proxigram [20]) is presented in Figure 1f and their detailed compositions are given in Table 1. The oxygen concentration is lower than the expected stoichiometry of oxides, such as  $\text{TiO}_2$  and  $(\text{Ti,Ta})_2\text{O}_5$ . This can be ascribed either to a metastable state of the oxide or to an underestimation of oxygen content due to loss in detection of oxygen ions [21,22]. Interestingly, the carbon content was dramatically decreased from 47.40 at.% initially to 2.3 at.% in the  $\text{TiO}_2$  and 1.1 at.% in  $(\text{Ti,Ta})_2\text{O}_5$ , confirming the oxidation of the MC carbides after 50 hours at 750 °C.

It has been suggested that substantial volume expansion due to the oxidation of MC carbides can result in localised plastic deformation [3,18], which was confirmed here by HR-EBSD performed in the vicinity of an oxidised MC carbide. First, a backscattered-electron micrograph of the polished cross-section of the specimen containing a partially oxidised MC carbide is shown in Figure 2a. The carbide is not entirely oxidised as observed by the distinct changes in contrast within the particle. The part of the carbide furthest from the surface appears unaffected by the exposure at 750 °C. In addition, recrystallisation only around the oxidised carbide was observed. The recrystallisation was confirmed by HR-EBSD as shown in Figure 2b, where the inverse pole figure map is given. During exposure at elevated temperatures, and below the protective oxide

scale at the surface, a  $\gamma'$  denuded zone forms, in which recrystallisation is often observed [10]. However, in our case, recrystallisation is only present close to the oxidised carbide and not along the entire length of the specimen surface, although a thin oxide layer is readily visible at the surface. This observation implies that the  $\gamma'$  dissolution and the subsequent recrystallisation is not directly related to the formation of a protective oxide scale, but instead is facilitated by the raised dislocation density produced by localised plasticity that is a direct consequence of the volume expansion of the oxidised MC carbide.

In Figure 2c, the geometrically necessary dislocation (GND) density map reveals a high GND density area around the carbide, up to approximately  $10^{15}$ – $10^{16}$  m<sup>-2</sup>. This area extends down more than 4  $\mu$ m below the surface and can be attributed to the volume expansion during the oxidation of the MC carbide. Narrow veins of high GND density can be seen between the recrystallised grain and the  $\gamma/\gamma'$  microstructure. It has been shown that regions with thermal strains are produced after the full heat treatment process around MC carbides in IN792 alloy. However, these regions extend only up to approximately 1  $\mu$ m from the carbides [4]. Thus, we believe that the observed high GND density shown in Figure 2c is mainly due to the volume expansion of the carbide during its oxidation. Due to the complex structure and combination of different oxides as shown in Figure 1e, any calculation of the volume expansion factor is difficult. However, the volume expansion factor of a Nb-rich MC carbide oxidising to Nb<sub>2</sub>O<sub>5</sub> has been estimated to be over 2 and we can expect similar factor here [18]. Finally, a high GND density is observed in the  $\gamma$  channels between the non-dissolved  $\gamma'$  precipitates as indicated by the black arrows in Figure 2c.

First, we investigate the dissolution of the  $\gamma'$  precipitates. Previously, the enhancement of the kinetics of the dissolution of  $\gamma'$  precipitates due to high dislocation density has been reported in a single crystal nickel-based superalloy [23]. An APT reconstruction from a specimen prepared from a region of the  $\gamma/\gamma'$  microstructure exhibiting a high GND density region is illustrated in Figure 3a. The reconstruction contains two  $\gamma'$  precipitates and their interfaces with the  $\gamma$  matrix. Besides, within the  $\gamma'$  precipitates,  $\gamma$  particles that result from the applied heat treatment conditions are present [24,25]. The interesting observation in this reconstruction is the tubular features within the  $\gamma'$  precipitates, which correspond to elemental segregation to dislocations. Segregation of certain elements to dislocations has previously been revealed by APT [26] and confirmed by correlative transmission electron microscopy / APT studies [27–31] or field ion microscopy [32]. A cylindrical region of interest perpendicular to the dislocation as shown in Figure 3a (arrow #1) reveals segregation of chromium and cobalt at the dislocations, whereas nickel, aluminium and titanium are depleted as shown in Figures 3b. Recently, it was shown for two nickel-based superalloys that this segregation of chromium and cobalt was indicative of pipe diffusion along the dislocations [33]. Such segregation to dislocations alters the local chemistry of the  $\gamma/\gamma'$  microstructure. In particular, dislocations leach chromium and cobalt from the  $\gamma$  matrix resulting in an increase of nickel solubility which eventually results in the dissolution of the  $\gamma'$  precipitates and the observed recrystallisation [29].

The above observation not only describes the dissolution of the  $\gamma'$  precipitates but also rationalises the composition of the recrystallised region, which differs substantially from the composition of the  $\gamma$  matrix. APT analysis was performed in three critical locations around the oxidised carbide of Figure 2a, as denoted by the yellow square boxes in the schematic illustration in Figure 4a. For instance, in Figure 3b an APT dataset from a recrystallised region reveals substantial increase of the nickel content from 45.7 at.% to 75.7 at.% in the recrystallised region. Besides, chromium dramatically decreases from 30.2 at.% to 7.9 at.%, whereas cobalt drops from 16.0 at.% to 10.7 at.%. The aluminium content was found not be altered. The detailed composition is given in Table 2. The composition of the recrystallised region is different to that of the  $\gamma$  matrix with a lower content of solution strengthening elements, thus it will be denoted as  $\gamma_R$ . It is expected from its composition, that  $\gamma_R$  is softer than the typical  $\gamma$  matrix allowing dislocations to move within the recrystallised regions more easily and would not oppose the initiation or propagation of cracks. That explains the high GND density within the recrystallised grains as shown in Figure 2c, and their accumulation towards the  $\gamma_R/\gamma'$  interface. This accumulation could also lead to the nucleation of cracks at that interface between the soft recrystallized  $\gamma_R$  and the harder  $\gamma/\gamma'$  microstructure.

Second, in order to investigate how the composition of the  $\gamma_R$  varies between the recrystallised grains, APT analysis was performed in various portions of the recrystallised region. In Figure 3c, an APT reconstruction

containing an interface between a  $\gamma'$  precipitate from the virgin microstructure and  $\gamma_R$  is displayed. Nitrides were found to form at or near the  $\gamma_R/\gamma'$  interface and within the  $\gamma'$  precipitate. Their composition is given in Table 3. These small nitride particles were found to be enriched with titanium, whereas a substantial amount of chromium (~10 at.%) was also measured. Their stoichiometry does not yet exactly correspond to TiN nitrides often observed in nickel-based superalloys [34]. This could be due to the short time of thermal exposure, which was not sufficient for the complete formation of TiN. Similar nitrides were observed previously to form in other nickel-based superalloys during the oxidation of MC carbides [35]. It is believed that the presence of brittle nitrides at that particular interface can also facilitate crack initiation and propagation.

Finally, a third APT reconstruction containing a  $\gamma_R/\gamma'$  interface from the third different  $\gamma_R$  is shown in Figure 3d. Atom probe crystallography analysis [36] reveals two sets of planes from the same crystallographic directions on either side of the interface, as shown in Figure 3d. This observation directly confirms the change in orientation between the  $\gamma'$  precipitate and the  $\gamma_R$  and hence that the  $\gamma'$  precipitate is located within the non-recrystallised region and not within the  $\gamma_R$ . A complete summary of the compositions of  $\gamma_R$  measured by APT is given in Table 2, which indicates no significant variations across different datasets. The composition of  $\gamma_R$  makes these soft regions susceptible to crack initiation.

The combined presence of an oxidised carbide and soft recrystallised grains will have a deleterious effect on the crack initiation life of polycrystalline nickel-based superalloys. In the case of external applied loads, micro-cracks can initiate from the oxide at the surface, that are sometimes porous, and can then propagate within the bulk [37,38]. For instance, it was shown under OP-TMF thermal-mechanical fatigue conditions that cracks initiate from oxidised MC carbides and propagate in a transgranular manner in single-notched cylindrical specimens of IN792 [4]. The strong accumulation of defects induced by the volume expansion of the oxidised carbide within the softer, finer microstructure in its vicinity is also likely to facilitate crack nucleation. Thus, the precipitation of this type of carbide needs to be carefully controlled. First, the volume fraction and the shape of the MC carbides should be considered. It is apparent that the number of crack initiation sites will increase as the volume fraction of this type of carbide increases. Thus, careful selection of the carbon content in superalloys can improve the crack initiation life under fatigue conditions. The shape of the MC carbides may also influence the crack initiation life. Intragranular script-type MC carbides can serve as sharp oxide intrusions from which cracks can propagate more rapidly. A combination of casting conditions and careful selection of compositions that control MC carbides formation can result in more desirable blocky MC carbides [39,40]. In addition, the chemistry of the MC carbide can play a significant role on its oxidation. For instance, a Nb-rich MC carbide will oxidise more easily compared to a Ti-rich MC carbide under the same exposure conditions, based on the free energy of formation of their corresponding oxides. As a consequence, crack initiation life will be shorter in the case of superalloys containing Nb-rich MC carbides.

In summary, our findings provide new insights on the crack initiation mechanism occurring consequently to the oxidation of MC carbides in polycrystalline superalloys. It was confirmed by HR-EBSD analysis that oxidation of MC carbides connected to the surface of polycrystalline superalloys results in regions with high GND density, due to volume expansion of the, often observed porous, oxidised carbide. In such regions, the dissolution kinetics of the  $\gamma'$  precipitates is enhanced due to chromium and cobalt transport via pipe diffusion at dislocations. As a consequence, soft recrystallised regions with limited amounts of solute strengthening elements form in the vicinity of oxidised MC carbides. The concurrent presence of hard but porous oxidised MC carbides and soft recrystallised  $\gamma_R$  regions will decrease dramatically the crack initiation life of polycrystalline superalloys. Thus, the volume fraction of MC carbides needs to be considered with extreme care during the design of new polycrystalline superalloys.

## Acknowledgements

The authors thank Siemens Industrial Turbomachinery AB, Sweden for the provision of the material. Uwe Tezins and Andreas Sturm are also acknowledged for their support on APT experiments.

## References

- [1] P.S. Karamched, A.J. Wilkinson, *Acta Mater.* 59 (2011) 263–272.
- [2] L.H. Rettberg, T.M. Pollock, *Acta Mater.* 73 (2014) 287–297.
- [3] A. Pineau, D.L. McDowell, E.P. Busso, S.D. Antolovich, *Acta Mater.* 107 (2016) 484–507.
- [4] P. Kontis, D.M. Collins, S. Johansson, A.J. Wilkinson, J.J. Moverare, R.C. Reed, in: *Superalloys 2016 13th Int. Symp.*, 2016, pp. 763–772.
- [5] P.A.S. Reed, *Mater. Sci. Technol.* 25 (2009) 258–270.
- [6] A.J. Wilkinson, D. Randman, *Philos. Mag.* 90 (2010) 1159–1177.
- [7] J. Nye, *Acta Metall.* 1 (1953) 153–162.
- [8] P. Kontis, E. Alabort, D. Barba, D.M. Collins, A.J. Wilkinson, R.C. Reed, *Acta Mater.* (2017).
- [9] T. Zhang, D.M. Collins, F.P.E. Dunne, B.A. Shollock, *Acta Mater.* 80 (2014) 25–38.
- [10] S. Pedrazzini, D.J. Child, G. West, S.S. Doak, M.C. Hardy, M.P. Moody, P.A.J. Bagot, *Scr. Mater.* 113 (2016) 51–54.
- [11] P. Kontis, S. Pedrazzini, Y. Gong, P.A.J. Bagot, M.P. Moody, R.C. Reed, *Scr. Mater.* 127 (2017) 156–159.
- [12] D.J. Larson, P.J. Maziasz, I.-S. Kim, K. Miyahara, *Scr. Mater.* 44 (2001) 359–364.
- [13] L. Viskari, M. Hörnqvist, K.L. Moore, Y. Cao, K. Stiller, *Acta Mater.* 61 (2013) 3630–3639.
- [14] K. Stiller, L. Viskari, G. Sundell, F. Liu, M. Thuvander, H.-O. Andrén, D.J. Larson, T. Prosa, D. Reinhard, *Oxid. Met.* 79 (2012) 227–238.
- [15] Y. Gong, D.J. Young, P. Kontis, Y.L. Chiu, H. Larsson, A. Shin, J.M. Pearson, M.P. Moody, R.C. Reed, *Acta Mater.* 130 (2017) 361–374.
- [16] K. Thompson, D. Lawrence, D.J. Larson, J.D. Olson, T.F. Kelly, B. Gorman, *Ultramicroscopy* 107 (2007) 131–9.
- [17] L. Matavelli Suave, J. Cormier, P. Villechaise, D. Bertheau, G. Benoit, F. Mauget, G. Cailletaud, L. Marcin, *Superalloys 2016 Proc. 13th Int. Symp. Superalloys* (2016) 747–756.
- [18] T. Connolley, P.A.S. Reed, M.J. Starink, *Mater. Sci. Eng. A* 340 (2003) 139–154.
- [19] H.T. Pang, P.A.S. Reed, *Mater. Sci. Eng. A* 448 (2007) 67–79.
- [20] O.C. Hellman, J.A. Vandenbroucke, J. Rüsing, D. Isheim, D.N. Seidman, *Microsc. Microanal.* 6 (2000) 437–444.
- [21] E.A. Marquis, N.A. Yahya, D.J. Larson, M.K. Miller, R.I. Todd, *Mater. Today* 13 (2010) 34–36.
- [22] B. Gault, D.W. Saxey, M.W. Ashton, S.B. Sinnott, A.N. Chiaramonti, M.P. Moody, D.K. Schreiber, *New J. Phys.* 18 (2016) 33031.
- [23] R. Giraud, Z. Hervier, J. Cormier, G. Saint-Martin, F. Hamon, X. Milhet, J. Mendez, *Metall. Mater. Trans. A Phys. Metall. Mater. Sci.* 44 (2013) 131–146.
- [24] M. Segersäll, P. Kontis, S. Pedrazzini, P.A.J. Bagot, M.P. Moody, J.J. Moverare, R.C. Reed, *Acta Mater.* 95 (2015) 456–467.
- [25] V. Yardley, I. Povstugar, P.-P. Choi, D. Raabe, A.B. Parsa, A. Kostka, C. Somsen, A. Dlouhy, K. Neuking, E.P. George, G. Eggeler, *Adv. Eng. Mater.* 18 (2016) 1556–1567.
- [26] D. Blavette, E. Cadel, A. Fraczkeiwicz, A. Menand, *Science* (80-. ). 286 (1999) 2317–2319.
- [27] B. Gault, M.P. Moody, J.M. Cairney, S.P. Ringer, *Mater. Today* 15 (2012) 378–386.
- [28] G.D.W. Smith, D. Hudson, P.D. Styman, C.A. Williams, *Philos. Mag.* 93 (2013) 3726–3740.
- [29] M. Kuzmina, M. Herbig, D. Ponge, S. Sandlobes, D. Raabe, *Science* (80-. ). 349 (2015) 1080–1083.
- [30] K.S. Chan, *Metall. Mater. Trans. A Phys. Metall. Mater. Sci.* 46 (2015) 2491–2505.
- [31] A. Kwiatkowski da Silva, G. Leyson, M. Kuzmina, D. Ponge, M. Herbig, S. Sandlobes, B. Gault, J. Neugebauer, D. Raabe, *Acta Mater.* 124 (2017).
- [32] J. Wilde, A. Cerezo, G.D. Smith, *Scr. Mater.* 43 (2000) 39–48.
- [33] P. Kontis, Z. Li, D.M. Collins, J. Cormier, D. Raabe, B. Gault, *Scr. Mater.* 145 (2018) 76–80.
- [34] S. Pedrazzini, E.S. Kiseeva, R. Escoubé, H.M. Gardner, J.O. Douglas, A. Radecka, P.M. Mignanelli, G.M. Hughes, G. Chapman, P.D. Edmondson, H.J. Stone, D. de Lille, P.A.J. Bagot, *Oxid. Met.* (2017) 1–20.
- [35] J. Litz, A. Rahmel, M. Schorr, *Oxid. Met.* 30 (1988) 95–105.
- [36] B. Gault, M.P. Moody, J.M. Cairney, S.P. Ringer, *Mater. Today* 15 (2012).
- [37] Z.W. Huang, Z.G. Wang, S.J. Zhu, F.H. Yuan, F.G. Wang, *Mater. Sci. Eng. A* 432 (2006) 308–316.
- [38] R.A. Kupkovits, R.W. Neu, *Int. J. Fatigue* 32 (2010) 1330–1342.
- [39] J. Chen, J.H. Lee, C.Y. Jo, S.J. Choe, Y.T. Lee, *Mater. Sci. Eng. A* 247 (1998) 113–125.

## Tables

Table 1: Summary of chemical compositions of the MC carbide after full heat treatment and after isothermal exposure in air at 750 °C for 50 hours as measured by atom probe tomography (at.%).

	<b>C</b>	<b>Ni</b>	<b>Cr</b>	<b>Al</b>	<b>Ti</b>	<b>Ta</b>	<b>Mo</b>	<b>W</b>	<b>Hf</b>	<b>O</b>
MC	47.4	0.0	0.5	0.0	30.0	18.5	1.7	1.6	0.3	0.00
MC/TiO <sub>2</sub>	2.3	1.7	1.0	1.0	34.1	4.7	0.0	1.2	0.4	52.9
MC/(Ti,Ta) <sub>2</sub> O <sub>5</sub>	1.1	0.4	0.3	0.4	18.5	13.7	0.0	3.5	0.2	61.3

Table 2: Summary of chemical compositions of the  $\gamma_R$  recrystallised regions and the  $\gamma$  matrix after isothermal exposure in air at 750 °C for 50 hours as measured by atom probe tomography, corresponding to APT reconstructions in Figure 3 (at.%).

	<b>Ni</b>	<b>Co</b>	<b>Cr</b>	<b>Al</b>	<b>Mo</b>	<b>W</b>	<b>Ti</b>	<b>Ta</b>
$\gamma$ (a)	45.7	16.0	30.2	2.1	2.3	1.2	1.7	0.1
$\gamma_R$ (b)	75.7	10.7	7.9	1.7	1.3	1.0	0.6	0.6
$\gamma_R$ (c)	74.5	10.4	8.3	2.5	1.2	1.0	1.0	0.6
$\gamma_R$ (d)	72.0	12.3	8.0	1.3	1.0	2.3	1.3	1.0

Table 3: Summary of the chemical compositions of the nitrides observed after isothermal exposure in air at 750 °C for 50 hours as measured by atom probe tomography (at.%).

	<b>Ti</b>	<b>Cr</b>	<b>Mo</b>	<b>C</b>	<b>Ta</b>	<b>Ni</b>	<b>N</b>
Nitride in $\gamma'$	45.1	9.6	1.9	1.4	0.6	0.6	39.8
Nitride in $\gamma_R/\gamma'$ interface	45.2	9.7	2.0	1.5	0.8	0.5	39.6

## Figures

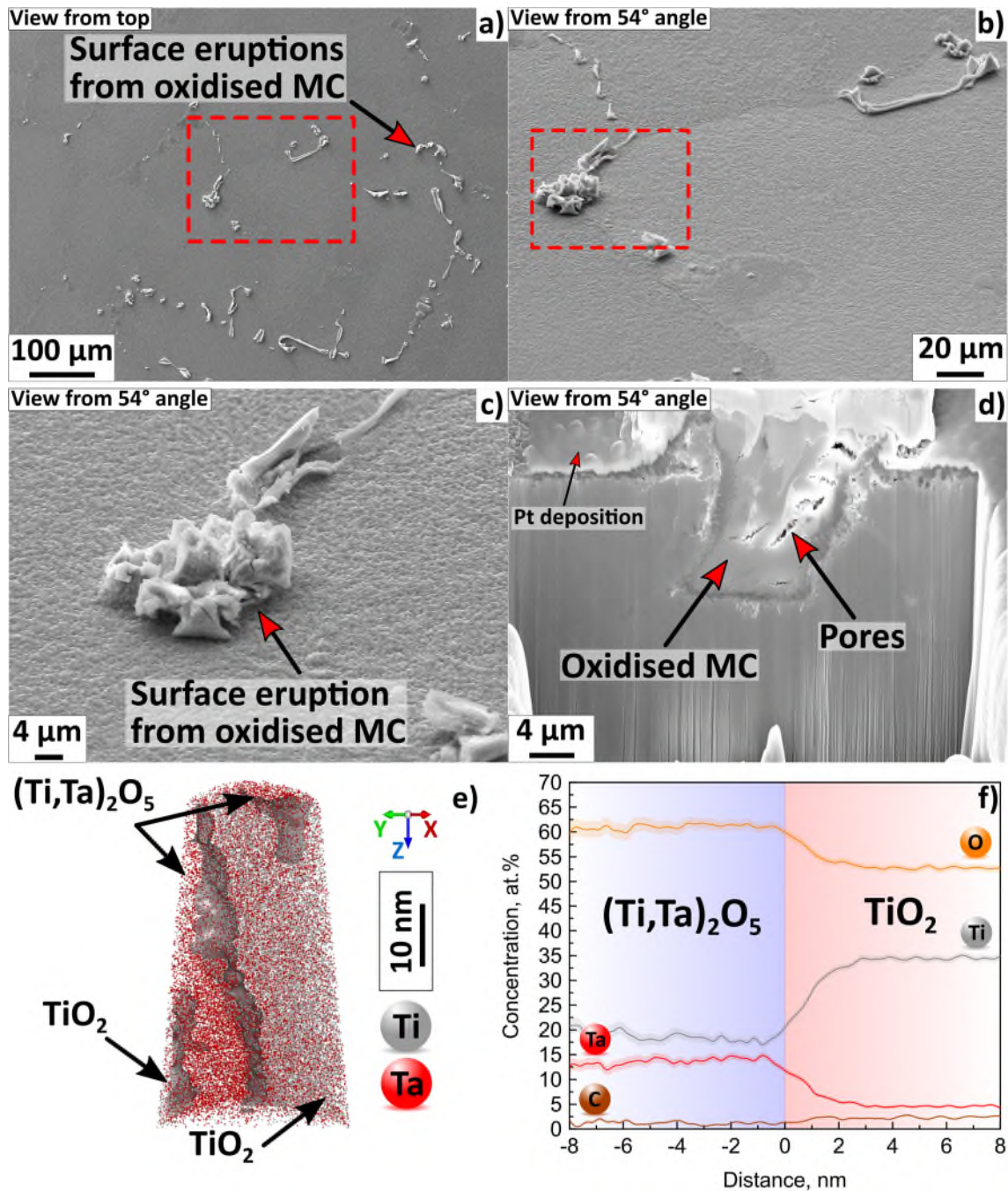


Figure 1: Secondary SEM micrographs showing: a) top view of surface eruptions from intergranular and intragranular oxidised MC carbides connected to the surface after isothermal static exposure in air at 750 °C for 50 hours, b) intergranular and intragranular oxidised MC carbides as denoted by the red dashed box in Figure 1a shown with the sample tilted 54° normal to the electron beam c) detail of surface eruption from the intergranular oxidised MC carbide denoted by the red dashed box in Figure 1b d) FIB section normal to the sample surface showing the oxidised MC carbide from Figure 1c within the bulk and the formation of pores after isothermal-static exposure in air at 750 °C for 50 hours, e) Atom probe reconstruction from an oxidised MC carbide, showing  $\text{TiO}_2/(\text{Ti,Ta})_2\text{O}_5$  interfaces within the oxidised carbide. The  $\text{TiO}_2/(\text{Ti,Ta})_2\text{O}_5$  interfaces are shown with an iso-concentration surface at 23.0 at.% Ti. f) Concentration profile across the  $\text{TiO}_2/(\text{Ti,Ta})_2\text{O}_5$  interface showing concentration of O, Ti, Ta and C. Error bars are shown as lines filled with colour and correspond to the  $2\sigma$  counting error.



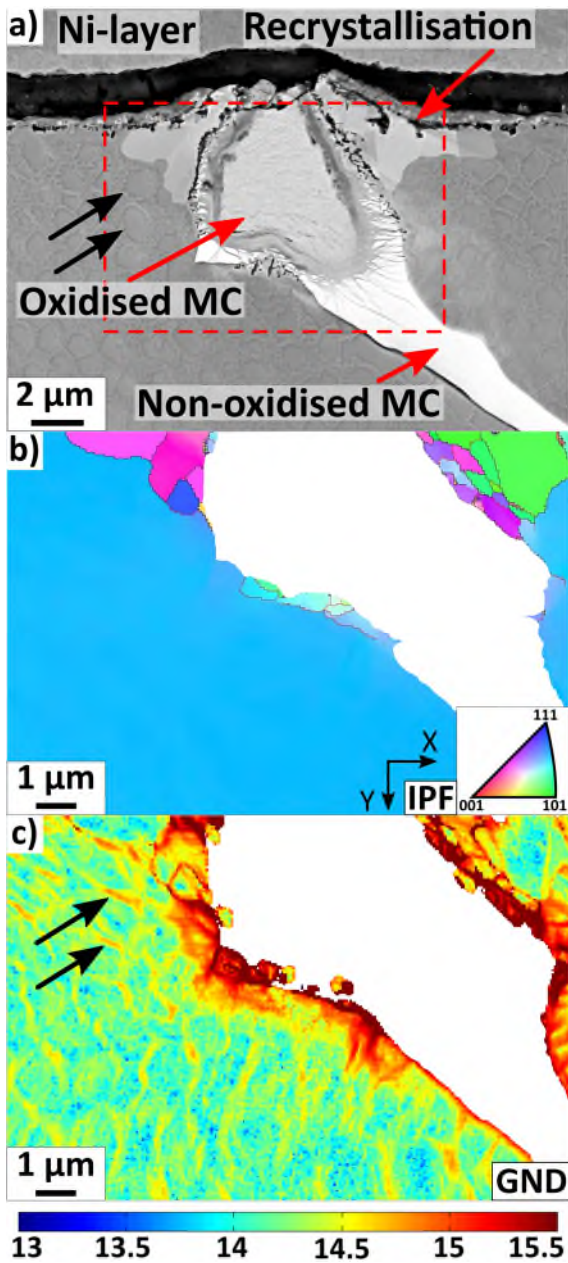


Figure 2: a) Backscattered SEM image showing recrystallisation in the vicinity of an intragranular oxidised MC carbide connected to the surface, b) EBSD inverse pole figure (IPF) map (reference vector in vertical Y direction) confirming the recrystallisation. The IPF map corresponds to the area denoted by the red dashed box and c) HR-EBSD strain map from the region as denoted in Figure 2a by the red dashed box, showing the geometrically necessary dislocation (GND) density map with the scale bar in  $\log_{10}$  scale of dislocation lines  $m^{-2}$ . Black arrows in Figure 2c indicate high GND density in  $\gamma$  channels and correspond to the black arrows in Figure 2a.



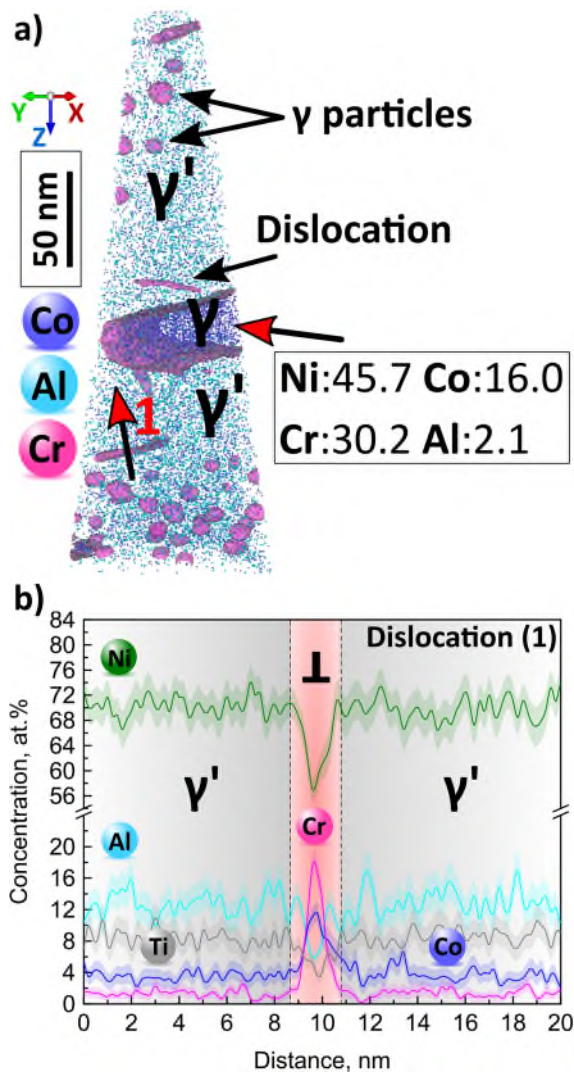


Figure 3: a) Atom probe reconstruction from a high GND density  $\gamma/\gamma'$  region next to an oxidised MC carbide, showing  $\gamma/\gamma'$  interfaces, dislocations and  $\gamma$  precipitates within the  $\gamma'$  precipitate. The  $\gamma/\gamma'$  interfaces and dislocations are shown with an iso-concentration surface at 3.0 at.% Cr. b) 1D concentration profile perpendicular to the denoted dislocation in Figure 3a (arrow #1). Error bars are shown as lines filled with colour and correspond to the  $2\sigma$  counting error.

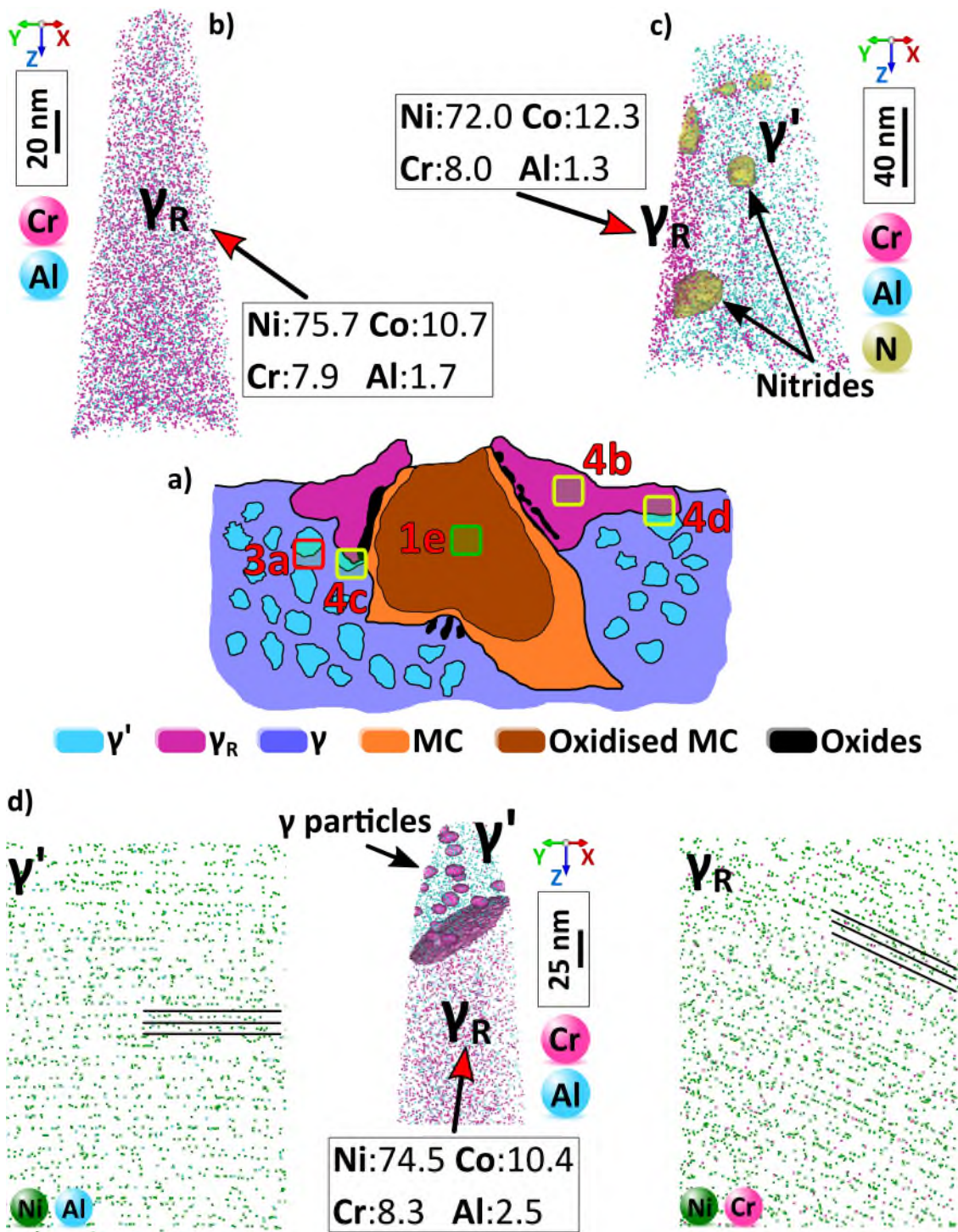


Figure 4: a) Descriptive schematic illustration (centre) of oxidised carbide from figure 2a alongside b) atom probe reconstruction within a  $\gamma_R$  recrystallised grain, c) atom probe reconstruction showing a  $\gamma_R/\gamma'$  interface, dislocations and  $\gamma$  precipitates within the  $\gamma'$  precipitate and nitrides at the  $\gamma_R/\gamma'$  interface and within the  $\gamma'$  precipitate. The  $\gamma/\gamma'$  interface and dislocations are shown with an iso-concentration surface at 3.9 at.% Cr and the nitrides are shown with an iso-concentration surface at 2.7 at.% N and d) atom probe reconstruction showing an interface between the non-recrystallised  $\gamma'$  and the  $\gamma_R$  recrystallised grain and  $\gamma$  precipitates within the  $\gamma'$  precipitate and analysis of the crystallographic planes perpendicular to the analysis direction of the non-recrystallised  $\gamma'$  and the  $\gamma_R$  recrystallised grain. The  $\gamma_R/\gamma'$  interface is shown with an iso-concentration surface at 3.0 at.% Cr. The yellow square boxes denote the location of each atom probe reconstruction in Figure 4, whereas the green and red boxes denote the location of the atom probe datasets from Figures 1e and 3a, respectively..